J. Fluid Mech. (2008), *vol.* 610, *pp.* 343–362.
doi:10.1017/S0022112008002759 Printed in the United Kingdom

Dynamics of volatile liquid droplets on heated surfaces: theory versus experiment

CHRISTOF SODTKE[1], VLADIMIR S. AJAEV[2] AND PETER STEPHAN[1]

[1]Darmstadt University of Technology, Petersenstrasse 30, 64287 Darmstadt, Germany

[2]Southern Methodist University, Dallas, TX 75275, USA

(Received 14 September 2007 and in revised form 21 May 2008)

We consider the evaporation of volatile liquid droplets deposited on a heated substrate in a pure saturated vapour environment. A mathematical model is developed that incorporates the effects of surface tension, evaporation, thermocapillarity, gravity, disjoining pressure, as well as unsteady heat conduction in the solid substrate. The apparent contact line is treated mathematically as a transition region between the macroscopic droplet shape and the adsorbed film of liquid on the heated substrate. Theoretical parametric studies are conducted to clarify the effects of thermocapillarity and wetting properties on the droplet dynamics. An experimental study is conducted in a closed container with de-ionized water droplets on a stainless steel foil heated by an electric current. The interface shapes are recorded together with the temperature profiles under the droplets, measured using thermochromic liquid crystals. Experiment and theory are in very good agreement as long as the conditions of applicability of our lubrication-type mathematical model are satisfied.

1. Introduction

Studies of volatile liquid droplets on heated solid substrates are important for many applications, such as spray cooling of electronics or coating of a solid substrate with a layer of another material. While the effects of capillarity and thermocapillary stresses on droplet dynamics have been studied extensively (see e.g. Braun *et al.* 1995 and references therein), relatively few studies address the effects of evaporation. Anderson & Davis (1995) and Hocking (1995) considered evaporating two-dimensional droplets on a uniformly heated substrate in the framework of the lubrication theory, valid when the droplet thickness is much smaller than its radius. The contact angle for such droplets is different from its equilibrium static value due to flow near the contact line and evaporation. Anderson & Davis (1995) suggested that each of these effects results in a small correction to the contact angle, compared to its static value, and therefore a linear combination of these corrections can be used to formulate the contact-angle condition for volatile droplets. The correction to the equilibrium value due to fluid flow was found based on experimental data for the case without evaporation.

An alternative approach to mathematical modelling of evaporating droplets is motivated by experimental studies of multilayer adsorbed films of vapour molecules formed on the surfaces of solid materials in equilibrium with vapour (see e.g. Derjaguin, Churaev & Muller 1987 for a review of experimental literature). When a droplet surface appears to come into contact with the solid substrate on a macroscopic

level, it may actually be in contact with this adsorbed film. This idea has been used by Ajaev (2005) to develop a model of spreading of volatile liquid droplets on uniformly heated surfaces. The moving contact line in this model is described as a localized region of rapid change of curvature in a manner similar to models of isothermal moving contact lines (de Gennes 1985), as well as several studies of steady menisci in the presence of evaporation, by e.g. Potash & Wayner (1972) and Moosman & Homsy (1980). We note that this approach does not require any modification of the classical no-slip condition and is therefore most appropriate for situations when a positive slip length is not expected, based on either experiments (Honig & Ducker 2007; Vinogradova & Yakubov 2003) or molecular dynamics simulations (Freund 2005).

Volatile droplets in vapour environment have been studied not only theoretically but also experimentally. Bourgés-Monnier & Shanahan (1995) studied thin droplets of water and *n*-decane on different surfaces in the presence of evaporation. They measured droplet radius and contact angle as functions of time. Gokhale, Plawsky & Wayner (2003) studied evaporation and condensation of droplets of *n*-butanol formed within a quartz cuvette that was partially filled with liquid and heated from either top or bottom. They carried out measurements of the radius of curvature of the droplet as a function of time in the regime when the droplet size slowly decreased due to evaporation.

A related problem of evaporation of droplets into air without external heating has been studied by e.g. Mollaret *et al.* (2004) and Hu & Larson (2005). The problem is, however, different in the sense that the main limiting mechanism of the evaporation process is the diffusion of vapour through air. A version of the same problem with solid particles suspended in the droplet was studied by Deegan *et al.* (2000) to explain the so-called 'coffee-ring' phenomenon, i.e. the brown ring left when a drop of coffee dries on a counter top.

While investigations of volatile droplets have been carried out by many researchers, two important issues are still unresolved. First, models of thin volatile droplets rely on simple (in most cases constant temperature) boundary conditions at the solid–liquid interface without consideration for heat conduction in the solid phase. Second, experimental and theoretical investigations have been developing in parallel without careful comparison between them for specific experimental systems.

In the present paper we develop a theory which is an extension of an earlier work on volatile droplets (Ajaev 2005) that incorporates three additional physical effects: (i) unsteady heat conduction in the solid under the droplet; (ii) heat losses to the gas phase above the liquid film; (iii) the effect of wetting properties of the liquid in the framework of a more general approach than in the earlier study. The theory, based on a lubrication-type description of the liquid flow, is developed for the case of an axisymmetric droplet in § 2. We then report an experimental study of evaporating droplets, carried out in a closed container filled with saturated vapour (§ 3 and § 4). Droplet shape data are obtained using optical methods, while temperature profiles under the droplet are recorded simultaneously using thermochromic liquid crystals (TLCs). The comparison between theory and experiment is presented in § 5, and we end with conclusions and discussion in § 6.

2. Mathematical model

2.1. *Formulation*

We consider an axisymmetric droplet of a volatile liquid of density ρ and viscosity μ on a heated rigid surface, as shown in figure 1. The droplet is placed on a heated foil of thickness d^* and thermal conductivity k_f. Here and below, the dimensional variables,

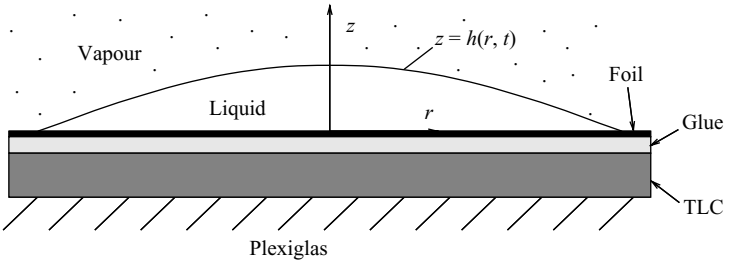

FIGURE 1. A sketch of a thin volatile axisymmetric liquid droplet on a multilayer substrate.

except for material properties such as k_f and μ, are labelled with stars. When liquid evaporates at the interface, the amount of heat supplied from the liquid side has to be sufficient to balance the latent heat of phase change and the heat loss into the vapour. The latter is typically much smaller than the former, so for the purpose of estimating the liquid flow velocity near the interface it can be neglected. Then, if we scale the length variables by d^* and the temperature by the equilibrium saturation temperature, T_S^*, the characteristic flow velocity near the interface can be estimated as

$$u_0^* = \frac{kT_S^*}{\rho \mathscr{L} d^*}. \tag{2.1}$$

Here k is the thermal conductivity of the liquid and $\mathscr{L}$ is the latent heat of vaporization per unit mass. Based on this velocity scale, we define the capillary number

$$Ca = \frac{\mu u_0^*}{\sigma_0}, \tag{2.2}$$

where σ_0 is the surface tension at the temperature T_S^*. Estimates show that the capillary number is typically small (on the order of 10^{-4} or less). However, this does not necessarily imply that viscous effects are negligible compared to the effects of capillarity. The two are equally important when the ratio of the droplet height to the radius of the wetted area on the substrate is of the order of $Ca^{1/3}$ (Anderson & Davis 1995). This thin-droplet limit is the focus of the present study, so we develop asymptotic expansions of the solutions for liquid flow and heat transfer in powers of $Ca^{1/3}$.

Let us choose the length scales for the liquid flow problem in the horizontal and vertical directions as $d^*Ca^{-2/3}$ and $d^*Ca^{-1/3}$, respectively; the resulting non-dimensional cylindrical coordinate system, (r, z), is shown in figure 1. We note that such scaling imposes limitations on droplet sizes. The experimental data are expected to match our theory only when the assumptions of the model are satisfied. The vapour–liquid interface in our formulation is represented by the function $z = h(r, t)$, where t is the time variable scaled by $d^*Ca^{-2/3}/u_0^*$. The non-dimensional velocity components in the radial and vertical directions, u and w, and the scaled pressure p are defined in terms of their dimensional counterparts according to

$$u = \frac{u^*}{u_0^*}, \quad w = \frac{w^*}{Ca^{1/3}u_0^*}, \quad p = \frac{p^*d^*}{\sigma_0 Ca}. \tag{2.3}$$

The governing equations for liquid flow in the droplet at the leading order take the usual lubrication-type form:

$$-p_r + u_{zz} = 0, \tag{2.4}$$

$$-p_z - Bo = 0, \tag{2.5}$$

$$r^{-1}(ru)_r + w_z = 0, \tag{2.6}$$

Here $Bo = \rho g d^{*2}/\sigma_0 Ca^{2/3}$ is the Bond number based on the droplet height, and g is the acceleration of gravity.

The leading-order non-dimensional temperature profile in the liquid is defined by

$$T_{zz} = 0. \tag{2.7}$$

Here and below all temperatures are scaled by the saturation temperature T_S^*. We assume that $u_0 d^*/\alpha_l$ is small (α_l is the thermal diffusivity of the liquid) and therefore the convective heat transfer in the liquid droplet is negligible. This is an important limitation of the present model.

The dynamics of liquid flow and heat transfer in the droplet is coupled to heat conduction in the solid substrate. Since the present theoretical work is motivated in part by experiments, we use a heat conduction model that corresponds to the experimental setup described in § 3. There are four layers of different solid materials under the droplet: heated foil, thin layer of glue, thermochromic liquid crystals (TLCs), and a Plexiglas plate, as shown in figure 1. (There is also a very thin (150–200 nm) layer of coating applied on the upper side of the foil to reduce the contact angle but it can be ignored without compromising the accuracy of heat conduction model.) The foil and the layers of glue and TLCs are very thin compared to the relevant horizontal length scales, so the equations for temperature profiles in the foil (T^f), in the glue (T^g), and in the TLCs (T^c) take the following simplified form,

$$T^f_{\hat{z}\hat{z}} + q = 0, \quad T^g_{\hat{z}\hat{z}} = 0, \quad T^c_{\hat{z}\hat{z}} = 0. \tag{2.8}$$

Here the generation of heat in the foil due to electric current is described by the constant density heat sources, q (scaled by $k_f T_S^* d^{*-2}$), $\hat{z} = z^*/d^*$, where z^* is the dimensional vertical coordinate. The Plexiglas plate is much thicker than the foil, so the plate thickness is scaled by $d^* Ca^{-1/3}$ and the equation for heat conduction there is in the form

$$T^p_t = \alpha T^p_{zz}, \tag{2.9}$$

where α is the thermal diffusivity of the Plexiglas scaled by $d^* u_0^*$. We note that while T^p_t is typically rather small, it may still be comparable to the right-hand side of (2.9) when T^p_{zz} is sufficiently small; this is indeed the case in many of our numerical simulations. At each interface between layers of different materials the temperatures and the normal components of the heat flux are continuous.

Let us now turn to the boundary conditions at the liquid–vapour interface. The fluid flow in the vapour phase directly above the liquid is in general coupled to the liquid flow in the droplet. However, in this study we use the one-sided model of evaporation of Burelbach, Bankoff & Davis (1988). It implies that the density and dynamic viscosity of the vapour phase are very small compared to those of the liquid. Therefore we take the limit when the corresponding non-dimensional ratios approach zero. However, the vapour density is retained in the boundary conditions where it multiplies the vapour velocity, which can be large. In order to include the non-dimensional evaporative mass flux J into the leading-order mass-conservation condition we scale the dimensional flux by $\rho u_0^* Ca^{1/3}$. With this choice and the above length and velocity scales, the non-dimensional leading-order conditions for conservation of mass and energy at the interface are written in the form

$$J + u h_r - w = -h_t, \tag{2.10}$$

$$J = -T_z - Bi(T - 1). \tag{2.11}$$

Equation (2.11) can be interpreted as the balance between the heat conducted through the droplet, the latent heat of the phase change at the interface, and heat loss to the vapour. The latter is characterized by the Biot number Bi, which is estimated based on the typical value of the Nusselt number for convective heat transfer in the vapour phase. Motivated by the experimental setup described in § 3, we assume that natural convection is the main mechanism of heat transfer in the vapour.

The normal stress condition at the interface includes contributions from capillarity and disjoining pressure:

$$p - p_v = -h_{rr} - r^{-1}h_r - \Pi(h), \tag{2.12}$$

where p_v is the non-dimensional vapour pressure. The vapour recoil term in the stress balance, discussed e.g. by Burelbach *et al.* (1988), is neglected in our model. We assume that the disjoining pressure $\Pi(h)$ is in the form

$$\Pi(h) = \frac{\varepsilon}{h^3} - D\mathrm{sech}^2\left(\frac{h}{l_0} - 2\right). \tag{2.13}$$

Here $\varepsilon = |A|/(\sigma_0 d^2)$, and A is the Hamaker constant. The first term in the expression for $\Pi(h)$ is the standard contribution due to the London–van-der-Waals dispersion forces, while the second one, first introduced by Wong, Morris & Radke (1992), represents one of the many different approximations of the effect of other components of disjoining pressure, e.g. due to electrostatic forces which can be more significant than the dispersion forces over a range of values of film thickness (Derjaguin *et al.* 1987). The choice of parameters D and l_0 and their relation to the wetting properties of the liquid are discussed in detail in Wong *et al.* (1992). The disjoining pressure is usually negligible except in the region of small h, where the transition between the macroscopic droplet shape and the adsorbed film takes place. This region is commonly referred to as *apparent* contact line, since on the macroscopic scale the liquid–vapour interface appears to come into contact with the solid surface there.

We assume that the surface tension is a linear function of temperature,

$$\sigma = \sigma_0 - \gamma(T^* - T_S^*), \tag{2.14}$$

and introduce the modified Marangoni number $Ma = \gamma T_S^*/\sigma_0$. With this choice, the shear stress condition at the interface is written as

$$u_z = -\overline{Ma}(T_r + h_r T_z), \tag{2.15}$$

where $\overline{Ma} = Ma\ Ca^{-2/3}$ is assumed to be an order-one quantity.

The scaled interfacial temperature T in the liquid is related to the local mass flux and pressure jump at the interface through the non-equilibrium condition, which can be written in the following form (Ajaev & Homsy 2001):

$$KJ = \delta(p - p_v) + T - 1, \tag{2.16}$$

where

$$K = \frac{\rho u_0^* \sqrt{2\pi R T_S^*/M}}{2\rho_v \mathscr{L} Ca^{-1/3}}, \qquad \delta = \frac{\sigma_0 Ca}{\mathscr{L}\rho d^*}. \tag{2.17}$$

Here R is the universal gas constant, M is the molar mass. According to (2.16), the departures of local temperature at the interface from the equilibrium value are characterized by two non-dimensional parameters, K and δ. The kinetic parameter, K, measures the relative importance of kinetic effects at the interface and is estimated based on the kinetic gas theory, as discussed in Schrage (1953). A more accurate

approximation developed by Rose (2000) results in an order-of-unity correction factor in the definition of K, but this factor is omitted here since it does not have a significant effect on the results of the present study. The parameter δ characterizes the effect of changes in liquid pressure on the local phase-change temperature at the interface.

Liquid flow and heat transfer in the droplet are coupled to heat conduction in the solid layers through the continuity of heat flux at the liquid–foil interface. This condition, together with heat flux balances at the foil–glue and glue–Plexiglas interfaces, allows us to find the relation between the vertical component of the temperature gradient at the top of the Plexiglas plate and the scaled evaporative mass flux J in the form

$$\frac{\partial T}{\partial z} = k_{fp}[\hat{q} - k_{lf}(J + BiT^i - Bi)], \tag{2.18}$$

where $k_{fp} = k_f/k_p$, $k_{lf} = k_l/k_f$, and $\hat{q} = q/C^{1/3}$. The temperature in the Plexiglas plate away from the foil is equal to the saturation temperature, so the non-dimensional boundary condition at the bottom of the computational domain is $T = 1$.

Finally, we note that at the solid–liquid interface the liquid velocity is zero. This boundary condition completes the mathematical formulation of the problem.

2.2. *Evolution equation*

The asymptotic model introduced in the previous section allows one to reduce the description of liquid flow to a single equation for droplet thickness, $h(r, t)$. The momentum equation (2.4) can be integrated twice to give the standard lubrication-type velocity profile. By substituting this profile into the mass-conservation condition, we obtain

$$h_t + J = \frac{1}{3r}(rh^3 p_r)_r + \frac{\overline{Ma}}{2r}\left[rh^2\left(\frac{\bar{T}^f - Jh}{1 + Bih}\right)_r\right]_r. \tag{2.19}$$

Here $\bar{T}^f$ is the scaled difference between the top of the foil and the saturation temperatures. Let us now express the scaled evaporative flux J in terms of $\bar{T}^f$ and the interface shape. The non-equilibrium condition at the interface, equation (2.16), relates J to the interfacial temperature. The latter can in turn be expressed in terms of $\bar{T}^f$, since according to the scaled heat conduction equation the temperature profile in the film is linear in z. This yields

$$J = \frac{\bar{T}^f - \delta[h_{rr} + r^{-1}h_r + \Pi(h)](1 + Bih)}{K + h + BiKh}. \tag{2.20}$$

Substituting this formula together with the expression for pressure in the liquid from the normal-stress balance, equation (2.12), into equation (2.19), results in the differential equation for the film thickness:

$$h_t + \frac{\bar{T}^f - \delta(1 + Bih)[h_{rr} + r^{-1}h_r + \Pi(h)]}{K + h + BiKh} + (3r)^{-1}[rh^3(h_{rr} + r^{-1}h_r + \Pi(h) - hBo)_r]_r$$
$$+ \frac{\overline{Ma}}{2r}\left[rh^2\left(\frac{\bar{T}^f(1 + Bih)^{-1} - \delta[h_{rr} + r^{-1}h_r + \Pi(h)]}{Kh^{-1} + 1 + BiK} - \frac{\bar{T}^f}{1 + Bih}\right)_r\right]_r = 0. \tag{2.21}$$

The boundary conditions for (2.21) are the two symmetry conditions at $r = 0$ and the conditions of zero first and second derivatives in the radial direction at $r = L$. The value of L has to be chosen large enough so that both the slope of the liquid–vapour interface and the radial temperature gradient remain negligible near $r = L$ at all stages of droplet evolution.

Evolution of the droplet thickness, $h(r, t)$, described by (2.21), is coupled to the heat conduction in the solid. Analysis of the quasi-steady heat transfer model formulated in (2.8) shows that with our scaling assumptions the temperature change across each of the thin layers of solid materials is negligible compared to the temperature drop across the droplet or the Plexiglas plate. Thus, it is sufficient to solve the equations for heat conduction in the liquid and in Plexiglas and then use continuity of temperature and the heat flux condition (2.18) to account for coupling between these two solutions. This approach is taken in the present study. The no-flux condition for the temperature field is applied at $r = L$.

To summarize, in order to find the droplet shape as a function of time one has to solve the evolution equation (2.21) simultaneously with equation (2.9) that describes unsteady heat conduction in the Plexiglas plate. The two equations are coupled together: the temperature profile $\bar{T}^f(r, t)$ that appears in (2.21) depends on heat conduction in the substrate, while the temperature gradient at the top of the Plexiglas plate is related to the evaporation rate through (2.18).

Numerical solution of the system of equations (2.9) and (2.21) is carried out using the finite-difference method with time-stepping performed by DVODPK solver, which is based on the standard DVODE package (Brown, Byrne & Hindmarsh 1989) but uses an iterative method for dealing with large linear systems which have to be solved at each time step in the discretized problem. In order to accurately describe rapid changes of the interface shape near the apparent contact line, local mesh refinement is carried out there by decreasing the mesh size by a factor of eight. As the contact line moves, the fine mesh is also shifted so that the point of maximum interfacial curvature stays near the centre of the fine mesh region.

The initial conditions for the numerical simulations presented in this section are as follows. Temperature in the solid plate is assumed to be initially uniform and equal to unity (corresponding to a situation when the solid is heated up after a prolonged contact with saturated vapour and is therefore at the saturation temperature). Constant curvature droplet of unit height (in scaled variables) is introduced at $t = 0$, placed on top of a uniform ultra-thin film of thickness 10^{-5}.

2.3. *Simulation results*

The numerical method allows us to track the evolution of the droplet shape and temperature field in the system for different values of non-dimensional parameters introduced in § 2.1. Two of these parameters, the ratios of thermal conductivities k_{fp} and k_{lf}, are not varied in experiments. Based on the values of thermal conductivities of the foil (stainless steel, $16.7\,\mathrm{W\,m^{-1}\,K^{-1}}$), water ($0.615\,\mathrm{W\,m^{-1}\,K^{-1}}$), and Plexiglas ($0.19\,\mathrm{W\,m^{-1}\,K^{-1}}$) we find $k_{fp} = 87.9$ and $k_{lf} = 3.68 \times 10^{-2}$. These values are used in all simulations in the present study. The Bond number is assumed to be negligible everywhere in this section, as appropriate for sufficiently small droplets, although the effects of gravity are included when comparison between theory and experiment is made in § 5.

2.3.1. *London–van-der-Waals disjoining pressure, negligible thermocapillarity*

Let us first consider the case when liquid is perfectly wetting under the isothermal conditions, i.e. the disjoining pressure is determined by London–van-der-Waals dispersion forces and in our scaled variables is given by (2.13) with $D = 0$. The parameter ε in this equation is a scaled version of the Hamaker constant, A. The latter depends on the properties of the liquid, the vapour, and the solid substrate and is generally rather difficult to measure. Fortunately, the numerical temperature

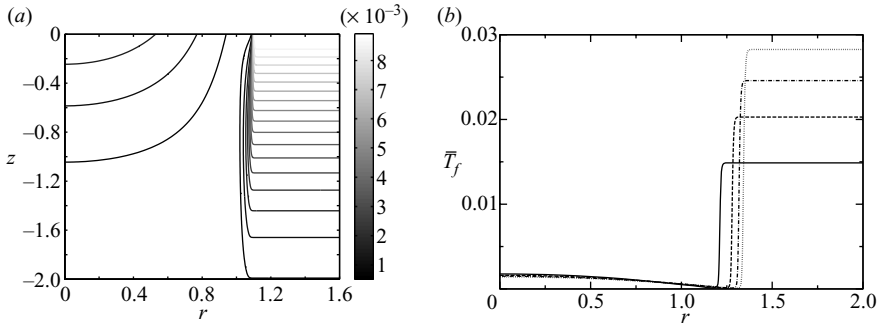

FIGURE 2. (*a*) Contour plot of temperature field in the Plexiglas plate for $t = 0.5$. (*b*) Temperature profiles under the droplet for $t = 2$ (solid line), $t = 4$ (dashed line), $t = 6$ (dot-dashed line), and $t = 8$ (dotted line).

profiles and macroscopic droplet shapes discussed below are not very sensitive to the choice of ε as long as its value is sufficiently small; all simulation results in this section are obtained for $\varepsilon = 10^{-6}$. We also found that solutions are not very sensitive to variations of parameter δ, allowing us to use the values of δ which are not as small as in actual experiments. Let us for now assume the effect of thermocapillarity to be negligible so that $\overline{Ma} = 0$ in (2.21). Other non-dimensional parameters used in the simulations in this subsection are $K = 10^{-3}$, $\delta = 10^{-5}$, $\alpha = 1$, $Bi = 10^{-4}$. While some of their values are very small, all of these parameters turn out to have a significant effect on the interface shape near the apparent contact line, i.e. for $h \ll 1$.

Let us discuss the numerical results for heat transfer in the system when the scaled density of heat sources is $\hat{q} = 10^{-4}$ (corresponding to the heater power of ~ 4 W in dimensional terms). This simulation was carried out in the domain of size $L \times L_v$, $L = 2$, $L_v = 5$; a uniform 201×201 mesh is introduced and then refined locally near $r = 1$. A temperature distribution in the Plexiglas plate at $t = 0.5$ is illustrated by a contour plot in figure 2(*a*) (the foil and droplet are above $z = 0$, not shown). The normal component of the heat flux on the boundary is non-zero only at the top of the plate where it is coupled to the evaporation rate through equation (2.18). The evaporative flux J in this equation is negligible when the top of the foil is macroscopically dry, corresponding to $r > 1.1$ in figure 2(*a*). Vapour above the foil in this region cannot provide a significant cooling effect since the value of the Biot number, Bi, is small, so most of the heat generated in the foil is used to heat up the substrate. As a result, a vertical temperature gradient is established, with temperature decaying to its initial value away from the foil (large $|z|$).

For $r < 1.1$, the situation is different: heat generated in the foil can be removed easily through the droplet due to evaporation, less heat goes into the Plexiglas, and the temperature there remains close to its initial value. This effect is most prominent in the region of small thermal resistance near the apparent contact line, as also seen in figure 2(*b*), showing temperature profiles under the droplet at four different moments in time. Away from the droplet, the substrate temperature increases with time while remaining nearly uniform in space, as one would expect if no droplet were present. The jump-like behaviour of the temperature profile near the apparent contact line clearly indicates that mathematical models based on the assumption of constant substrate temperature are not likely to accurately capture the evolution of the system, at least for relatively low-thermal-conductivity substrates such as Plexiglas. The situation is

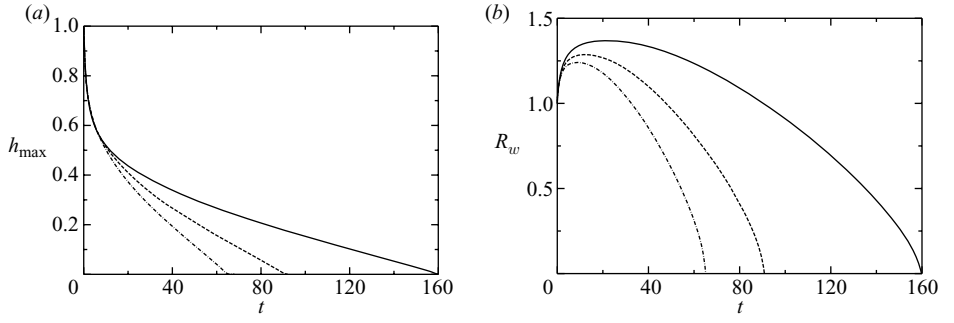

FIGURE 3. Droplet height (*a*) and radius (*b*) as functions of time for different values of the heating parameter: $\hat{q} = 10^{-4}$ (solid lines), $\hat{q} = 2 \times 10^{-4}$ (dashed lines), and $\hat{q} = 3 \times 10^{-4}$ (dot-dashed lines).

likely to be different for more conductive (e.g. metal) substrates since heat fluxes in such substrate can be larger than typical heat fluxes through the droplet.

Let us now discuss droplet shapes. The maximum height of the droplet is recorded as a function of time in figure 3(*a*) for three different values of $\hat{q}$, while figure 3(*b*) shows corresponding plots for the wetted radius, R_w. The latter is defined as the radial coordinate of the point of maximum curvature and can be interpreted as the radius of the apparent contact line, also called the 'droplet radius'. (The simulations were carried out with 601 mesh points in the vertical direction and $L_v = 40$.) Since the disjoining pressure is inversely proportional to the cube of film thickness, in the absence of evaporation the droplet would be spreading indefinitely due to capillary forces, with the inverse aspect ratio, $h_{\max}/R_w$ eventually approaching zero. Capillary-spreading-type behaviour is seen in figure 3 only at the initial stage of droplet evolution, when droplet height decreases rapidly and is essentially independent of $\hat{q}$, while R_w increases. Then, at $t \approx 10$ evaporation takes over, eventually leading to relatively slow (compared to evolution at the initial stage) decrease in both the height and the radius and preventing the inverse aspect ratio, $h_{\max}/R_w$, from rapidly decaying to zero. This is analogous to a steady-state situation when a finite contact angle is established due to evaporation even for liquids that are perfectly wetting under the isothermal conditions (Potash & Wayner 1972).

Comparison between different curves in figure 3(*b*) reveals that the parts of the curves that correspond to decreasing wetted radius ($R_w'(t) < 0$) can actually be transformed into each other by simple stretching/compression of both r and t. Let us try to understand the origin of such self-similar behaviour. Outside the small region near the apparent contact line, the droplet height is governed by an approximate equation in the form

$$h_t + J + (3r)^{-1}[rh^3(h_{rr} + r^{-1}h_r)_r]_r = 0. \tag{2.22}$$

Here the scaled flux J is related to $\hat{q}$ through (2.18). However, if we make a rough approximation assuming that J is proportional to $\hat{q}$, as appropriate when all heat generated in the foil under the droplet is used to evaporate the droplet, then a two-fold increase in $\hat{q}$ translates into a two-fold increase of J. If time and radial coordinate variables are transformed simultaneously according to $t \to t/2$, $r \to r/2^{1/4}$, then the approximate equation (2.22) does not change (i.e. it is invariant under this transformation). The numerical results obtained from equation (2.21) and shown in figure 3(*b*) indicate that at $R_w'(t) < 0$ the curve corresponding to $\hat{q} = 0.0001$ is transformed into

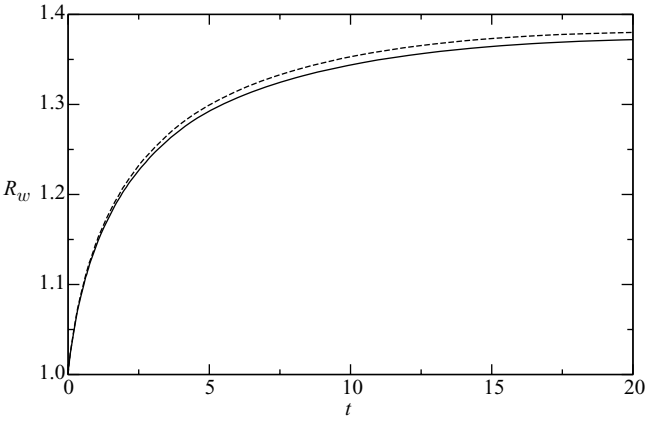

FIGURE 4. Droplet radius as a function of time for $K = 1.0$, $\overline{Ma} = 10$ (solid line) and $\overline{Ma} = 0$ (dashed line).

the curve corresponding to $\hat{q} = 0.0002$ when the variables are changed according to $t \to t/1.75$, $r \to r/1.06$. While there is clearly some quantitative discrepancy between this result and the prediction based on equation (2.22), the comparison is sufficiently good to justify the proposed explanation of self-similar dynamics, especially given a number of simplifying assumptions made in deriving the approximate equation (2.22). We note that the self-similar behaviour cannot be correctly captured by models based on the assumption of constant substrate temperature.

2.3.2. *The effect of thermocapillarity*

The effect of thermocapillary stresses is routinely neglected in the models of liquid–vapour interfaces based on the assumption of local thermodynamic equilibrium. The latter requires the interfacial temperature to be equal to its saturation value and therefore implies that there are no thermal gradients along the interface. However, it is important to emphasize that this argument is no longer valid when non-equilibrium effects are taken into account, resulting in the dependence of the interfacial temperature on the local evaporation rate. In the present study, the non-equilibrium effects at the interface are measured by the non-dimensional parameter K. We conducted numerical studies of droplet shape evolution over a range of values of K and the modified Marangoni number, Ma, and found that the effects of thermocapillarity for realistic values of Ma are very small unless the value of K is close to unity or higher. A typical plot of droplet radius versus time for $K = 1$ and $\overline{Ma} = 10$ (corresponding to $Ma \sim 0.1$) is shown in figure 4 (solid line). The result for $\overline{Ma} = 0$ is also shown by a dashed line for comparison; the values of all other parameters are the same as in the previous subsection. The temperature gradient along the interface is directed from the hotter region near the apparent contact line toward the colder region at the top of the droplet, so thermocapillarity results in smaller values of the droplet radius than predicted by the theory for $\overline{Ma} = 0$.

Droplet spreading and evaporation in the presence of thermocapillary stresses was previously studied under the assumption of uniform temperature of the solid substrate (Ajaev 2005). We found that for comparable droplet sizes and evaporation rates the present model predicts smaller temperature gradients near the apparent contact line (and therefore weaker thermocapillarity) than the previous study. This can be explained by the effect of heat conduction in the solid that tends to prevent

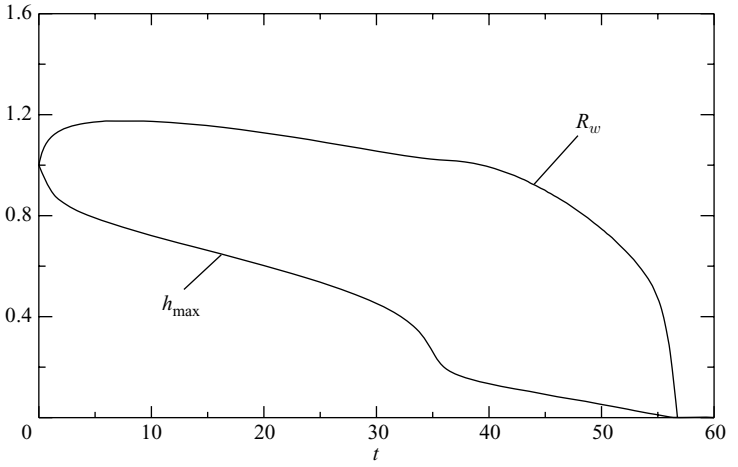

FIGURE 5. Droplet radius and height versus time for $D = 5.0$, $l_0 = 0.1$, $\hat{q} = 3 \times 10^{-4}$.

formation of localized regions of high-temperature gradients in the liquid near the apparent contact line.

The present model predicts that thermocapillary stresses not only affect the flow in the droplet but can also cause deformations of the vapour–liquid interface in the nearly flat ultra-thin film. However, it is important to keep in mind that our treatment of thermocapillarity is likely to break down on such small scale where the surface tension depends not only on the local temperature but also on the nature of surface forces acting on the film. Therefore, these deformations in the adsorbed film are not discussed here.

2.3.3. *Two-component disjoining pressure*

Figure 5 shows droplet height and radius as functions of time for $\hat{q} = 3 \times 10^{-4}$ and the general model of disjoining pressure given by (2.13) with $D = 5$, $l_0 = 0.1$; other parameter values are the same as in § 2.3.1. Equation (2.13) with $D > 0$ describes a situation when two components of disjoining pressure are present and the apparent contact angle is non-zero under the isothermal conditions, as discussed in Wong *et al.* (1992). Comparing the dot-dashed lines in figure 3 (that correspond to the one-component London–van-der-Waals model of disjoining pressure and $\hat{q} = 3 \times 10^{-4}$) and figure 5, we observe that in the latter case droplet height is larger and its radius is smaller throughout most of droplet evolution. This can be explained by larger values of the apparent contact angle, which can be estimated as a sum of its isothermal value and a correction due to evaporation (Anderson & Davis 1995). The isothermal contact angle in figure 3 is zero since the London–van-der-Waals model of disjoining pressure corresponds to liquids that are perfectly wetting under the isothermal conditions.

At the late stages of evolution (at $t \sim 40$ in figure 5) there is clearly a transition point where droplet radius changes from nearly constant to rapidly decaying. The rate of change of height at this point in time becomes nearly constant. The latter is approximately the same as the rate of change of h_{max} in figure 3, suggesting a simple explanation for the transition. The linear decay of $h_{max}(t)$ is recovered because the second component of disjoining pressure in (2.13) for such thin droplets is much smaller than the first one, so the dynamics is dominated by the London–van-der-Waals forces. The value of h_{max} corresponding to this transition is on the order of l_0 and therefore turns out to be rather small in most experiments with macroscopic

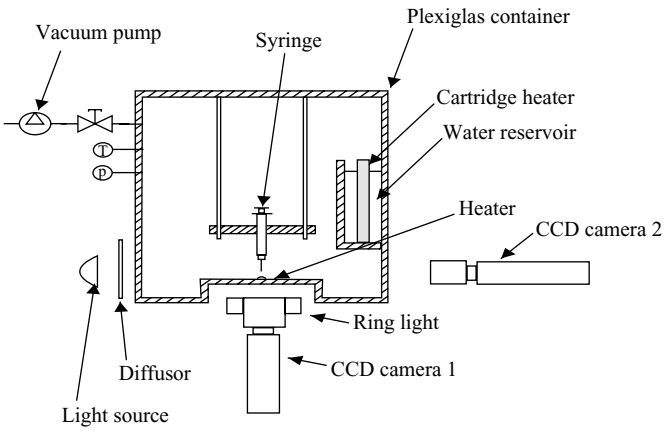

FIGURE 6. Schematics of the experimental setup.

droplets (we have chosen a relatively large l_0 in figure 5 to illustrate clearly the late stages of droplet evolution).

It is interesting to note that the nearly constant droplet radius over a significant time interval seen in figure 5 implies that the contact line at this stage can be considered 'pinned'. Contact line pinning is often explained in the literature by the effects of surface roughness or chemical defects. Our simulation results shown in figure 5 suggest that pinned-contact-line-type behaviour can be observed even on smooth homogeneous substrates, as a result of interplay between different components of disjoining pressure. The transition to rapid decay in droplet radius seen at the final stages of droplet evolution can then be interpreted as sudden de-pinning that is also often observed in experiments.

3. Experimental methods

We perform experiments to obtain data for droplets evaporating on a thin-foil heater. Evolution of both the temperature field on the heater and the droplet shape are investigated. To obtain the temperature field we use thermochromic liquid crystals (TLCs) applied to the lower surface of the foil heater, while the evolution of the droplet shape is observed simultaneously via the shadow method with a CCD camera. These are the main ideas leading to the setup which is described in the following subsection.

3.1. *Experimental setup*

A schematic of the experimental system is shown in figure 6. The experiments have been conducted in a closed Plexiglas container of size of 300 mm × 300 mm × 380 mm. In order to create a saturated vapour atmosphere, the experimental container is equipped with a reservoir for de-ionized water and a cartridge heater. A syringe (needle diameter 330 μm) filled with deionized water is used to generate single droplets, which can be either dropped or deposited on the heater where they evaporate. The syringe can be actuated from outside the experimental container.

A schematic of the heater is shown in figure 7. It consists of an electrically heated 10 μm thick stainless steel foil and a fixation system with springs to ensure a wrinkle-free heater surface. The heated surface has a size of 60 mm × 30 mm. A sheet of thermochromic liquid crystals is applied to the lower surface of the heating foil using a thin layer (40 μm) of a glue with a high thermal conductivity

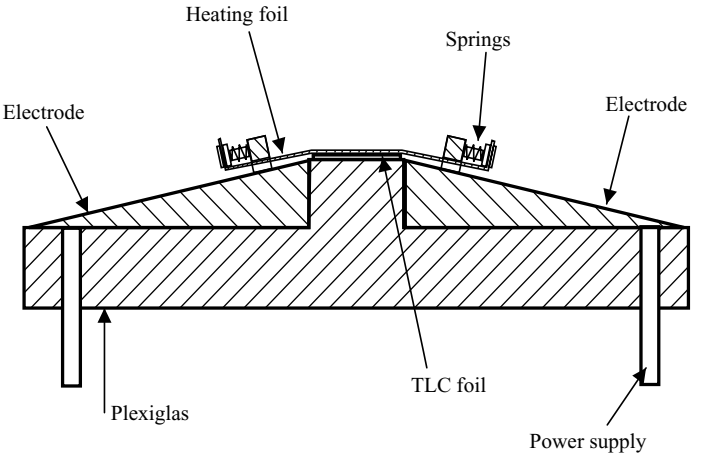

FIGURE 7. Schematics of the heater.

of ($k_g = 7\,\mathrm{W\,m^{-1}\,K^{-1}}$). TLCs reflect a distinct colour depending on their temperature when illuminated by white light. Below and above their active temperature range they are transparent so that only their black background coating can be observed. Within their working range the reflected light changes from red to green to blue with increasing temperature. Images of the TLCs are captured using a three-chip colour CCD camera (CCD camera 1 in figure 6). The colour information is converted from the RGB signal of the camera to the HSV colourspace (hue, saturation, value). In the HSV colourspace, the hue value is measured in degrees. It contains all the colour information and can therefore be used as a single value for the temperature measurement. An *'in situ'* calibration method for the TLCs has been developed, where the TLCs can be calibrated within the experimental setup, with the temperature of the TLCs being controlled via a thermostat. A correlation of hue value and temperature is obtained by measuring the temperature of the TLCs with thermocouples and simultaneously recording their colourplay. A 7th-order regression proved to be a good approximation for the correlation. The stainless steel foil is electrically heated with constant voltage and current, resulting in a constant heat flow density in the foil. Owing to the small thickness of the foil the temperature distribution on the back of the foil does not deviate significantly from that on the front of the foil. This has already been shown for a capillary slot experiment where the same foil has been used (Höhmann 2004). The TLCs are illuminated through the Plexiglas base plate of the heater with a ring light, which is connected to a cold light source. The TLC colourplay is acquired with a frame rate of 2 Hz. The spatial resolution of the TLC images is $14\,\mu\mathrm{m}^2$/pixel. Owing to the limited working bandwidth of TLCs, the pressure inside the Plexiglas container has to be controlled to ensure that the saturation temperature of water is well between the limits of the TLC working bandwidth. A vacuum pump is used to keep the pressure inside the Plexiglas container at 50 mbar (± 4 mbar) which relates to a saturation temperature of $33 \pm 2\,^{\circ}\mathrm{C}$. The pressure inside the container is monitored with a pressure transducer. The vapour temperature inside the container is measured with two thermocouples at different locations. The evolution of the droplet shape is observed horizontally from the side by means of a second CCD camera (CCD camera 2). To obtain images with sharp edges the droplets are lit with parallel back light. The

FIGURE 8. Image of droplet on heater.

images of the droplets are acquired with a frequency of 2 Hz. The spatial resolution of these images is 9 μm^2/pixel.

3.2. *Experimental procedure*

Before each set of experiments, the heating foil is cleaned with acetone and rinsed with de-ionized water. Afterwards, the heater is coated with a thin layer (150–200 nm) of a hydrophilic paint (Roehm GmbH & Co. KG, Germany) to reduce the contact angles to the values of 15° or below. Then the experimental container is evacuated down to 40 mbar and the cartridge heater is switched on. Experiments are started when the temperature inside the container reaches 32 °C and the pressure increases up to 50 mbar with the vacuum pump running continuously. At that point the power to the cartridge heater is reduced to maintain a constant temperature inside the experimental container. Both CCD cameras are started and a first droplet is generated using the syringe. The CCD cameras are stopped when the droplet has fully evaporated, which is decided by examining the images from both cameras. Then the image acquisition is started again and the next droplet is generated.

3.3. *Image processing*

The captured TLC images are processed using MATLAB to convert them into temperature profiles. Temperatures are measured along lines for which the starting and ending points are chosen based on the first TLC image. The same line is then used for the complete sequence. To reduce noise, an averaging filter over an area of 3×3 pixels is applied to the images before converting the hue values to temperatures. The uncertainty of the TLC temperature measurement is estimated to be within ± 0.5 °C, mostly due to the usage of encapsulated TLCs and a high spatial resolution which causes problems with the temperature measurement at the edges of the TLC capsules.

The droplet images are saved as grey-scale matrices and are also processed using MATLAB. Before each set of measurements, a reference image is acquired showing the heater without any droplet. To track the evolution of the diameter of the wetted area, droplet height, and apparent contact angle as the droplet evaporates, the steps described in the following are performed. First, the reference image is subtracted from each droplet image resulting in a new image that only contains the shape of the droplet and is black (has zero intensity) elsewhere. Then the contrast is enhanced and the wetting diameter is detected by finding the first column of the intensity matrix from the right and the left edge of the image that has a non-zero pixel. The distance between those columns is the diameter of the droplet in pixels. The diameter can easily be calculated based on the reproduction scale of the optics. To evaluate the droplet height from each image, the droplet is assumed to be symmetric. Therefore the height of the droplet is evaluated at the droplet centre by finding the first non-zero pixel at the corresponding column of the grey-scale matrix. To obtain the apparent contact angle of the droplet, the shape of the droplet is fitted with a conical section using the upper half of the circle equation, which has been proved to be a good approximation. An image of an evaporating droplet with the fitted conical section is shown in figure 8. The volume of the droplet is also calculated based on this equation. By performing the steps described above for every droplet image captured as a droplet evaporates, the evolution of the quantities of interest can be determined. The uncertainty in the

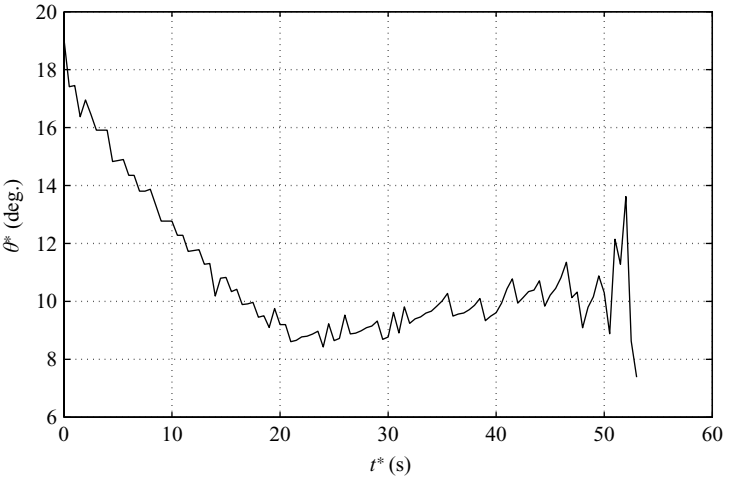

FIGURE 9. Evolution of apparent contact angle.

measurements obtained from the image processing is estimated to be up to 2 pixels per detected edge, leading to an uncertainty of $\pm 36\,\mu m$ for the diameter and $\pm 18\,\mu m$ for the droplet height. Furthermore, each droplet image can be related to a TLC image so that the corresponding temperature profile below the evaporating droplet can also be obtained.

4. Experimental results

Experiments have been conducted with different heating powers ranging from 1 W to 3 W. In addition, the initial size of the droplet (before it hits the substrate) was varied between 1 mm and 3 mm. The initial apparent contact angle was in the range of $10^\circ < \theta^* < 20^\circ$, despite the care taken when cleaning and coating the heater. This variance in the apparent contact angle might also be caused by a variation in the way the droplet was deposited, since the distance between syringe needle and heated surface varied according to the filling of the syringe by up to 20 mm. Additionally, impurities from the droplets might have agglomerated on the heater. All experiments show the same general behaviour of the droplets, independent of heating power and droplet size.

4.1. *Evolution of droplet shape*

In the following, results for a heating power of 2.5 W will be presented. As shown in figure 9, just after the droplet is deposited on the heating foil the apparent contact angle θ^* starts to decrease until it reaches a value of $\theta^* \approx 9^\circ$ after $t^* = 20\,s$. Then, the apparent contact angle increases slightly. However, this increase seems to be within the range of uncertainty of the measurement. In the last phase of the droplet lifetime rather large oscillations in θ^* can be observed. These oscillations are due to errors caused by the fitting algorithm and are triggered by the small droplet diameter and height during that phase.

Figure 10 shows the evolution of the droplet diameter D^* versus time t^*. As the droplet evaporates, the absolute rate of change of droplet diameter increases. Simultaneously, the droplet height h^* decreases. While the droplet height h^* strongly decreases with time t^* (see figure 11) as long as both apparent contact angle θ^* and droplet diameter D^* decrease, the change of droplet height h^* with time t^* slows

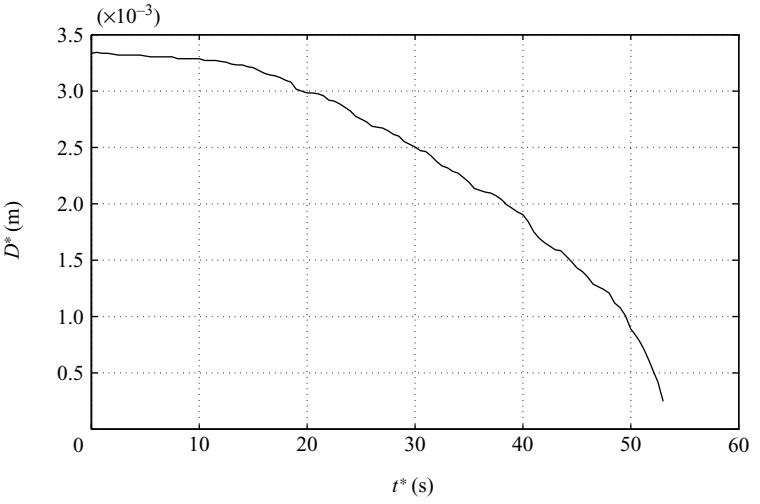

FIGURE 10. Evolution of droplet diameter.

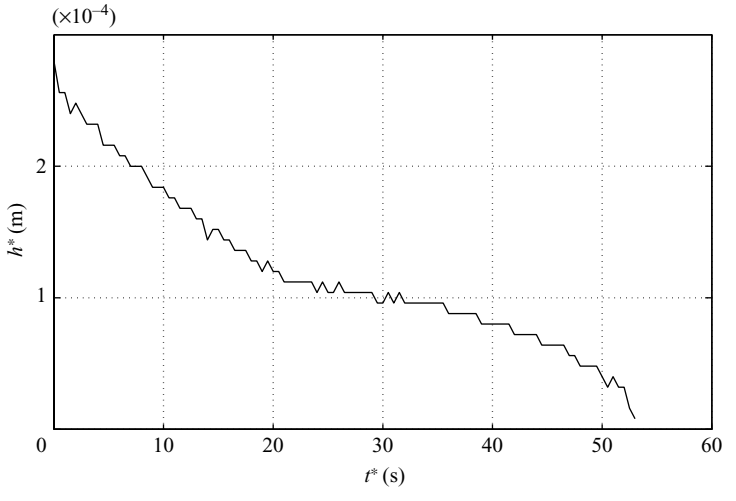

FIGURE 11. Evolution of droplet height.

down at $t^* \approx 20\,\mathrm{s}$, when the apparent contact angle θ^* remains constant while only the droplet diameter D^* reduces.

The change of droplet volume V^* with time t^* is shown in figure 12. After the droplet is deposited on the heater, its volume reduces fast as contact angle and diameter shrink. The change of volume with time slows down as more and more fluid evaporates and the droplet diameter reduces. Due to the reduced droplet diameter, less heat is transferred from the foil heater to the droplet, which results in a lower evaporation rate and hence in a slower change of droplet volume V^* with time t^*.

4.2. *Evolution of temperature*

Recoding the colour of the TLCs below an evaporating droplet allows us to obtain accurate measurements of temperature profiles. The TLCs reflect green light in the

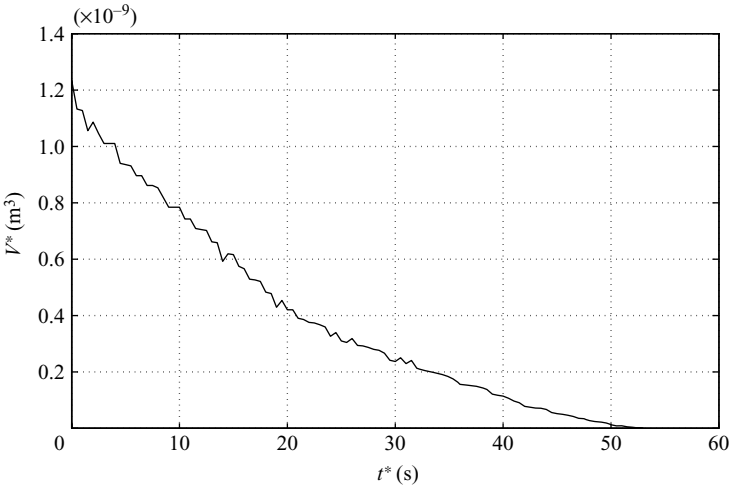

FIGURE 12. Evolution of droplet volume.

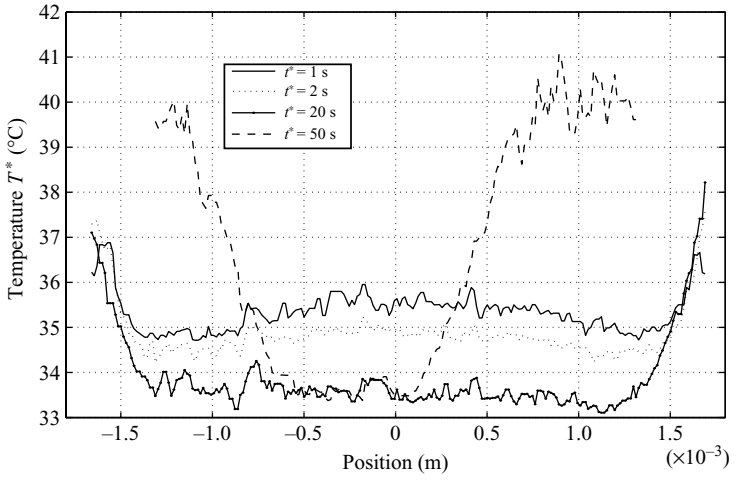

FIGURE 13. Evolution of temperature distribution beneath the evaporating droplet.

area under the droplet. This green changes to blue and then to black with increasing distance from the droplet centre, indicating that the temperature rises.

The temperature profile under an evaporating droplet at four different times ($t^* = 1$ s, $t^* = 2$ s, $t^* = 20$ s, $t^* = 50$ s) after the droplet was deposited on the surface is displayed in figure 13. It shows for all cases an almost constant temperature underneath the droplet and a strong temperature rise within a length of less than 0.2×10^{-3} m in the direction of the adsorbed film area of the heating foil. During the first seconds after the droplet is deposited on the heating foil, the temperature underneath the droplet reduces fast. The change of temperature is less pronounced for the later stages of evaporation, as can be seen in figure 13. Within the first two seconds after the droplet is deposited on the heater, the temperature changes by an average of $\Delta\bar{T}_h^* \approx 0.5\,^\circ$C below the droplet, while the temperature change is $\Delta\bar{T}_h^* \approx 1.1\,^\circ$C between $t^* = 2$ s and $t^* = 20$ s and only $\Delta\bar{T}_h^* \approx 0.05\,^\circ$C between $t^* = 20$ s and $t^* = 50$ s.

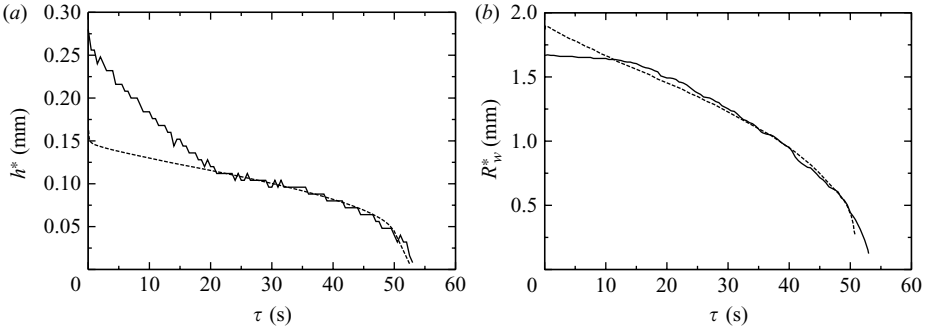

FIGURE 14. Dimensional droplet height (*a*) and wetted radius (*b*) as functions of time computed from the mathematical model (dashed line) and measured experimentally (solid line).

5. Comparison between theory and experiment

Let us now compare the results obtained from the mathematical model of § 2 and the experimental measurements discussed in § 4. Based on the parameters of our experimental setup, the non-dimensional constants of the model are $K = 2.2 \times 10^{-3}$, $\delta = 2.9 \times 10^{-6}$, $\alpha = 1.3$, $Bi = 1.3 \times 10^{-4}$, $Bo = 0.01$, $\hat{q} = 6.2 \times 10^{-5}$; the effect of Marangoni stresses is negligible. There are no accurate data for disjoining pressure parameters for water on the coated surface used in experiments, but, as discussed above, our model is not very sensitive to the changes in the scaled Hamaker constant, ε, as long as the latter remains sufficiently small. The wetting properties of water on the coated foil surface in our model are controlled by the parameters D and l_0 in the disjoining pressure formula, (2.13). The values of the latter are chosen based on the experimentally observed values of the apparent contact angle and are kept constant during the simulation. While the simulation produces results in non-dimensional form, the values of physical variables can be easily recovered using the definition of scales provided in § 2.1. A typical comparison between theory and experiment for droplet height is shown in figure 14(*a*). The solid line corresponds to experimental data and the dashed line is the prediction of the model. Comparison between the experimental and theoretical values of the dimensional droplet radius, R_w^*, is shown in figure 14(*b*).

The initial discrepancy between theory and experiment seen in figure 14 is due to the fact that our lubrication-type theory is not valid immediately after the impact when the dimensional aspect ratio of the droplet is not sufficiently large. In fact, the experimental recording of the droplet shape starts when the aspect ratio is just 5, while the model requires it to be close to $C^{-1/3} \sim 23.2$. After $\tau \sim 20$ s the thin-droplet regime is established and the agreement between theory and experiment is clearly very good.

Our numerical temperature profiles indicate that the dimensional temperature near $\tau \sim 50$ s is expected to be close to 33.3 °C everywhere under the droplet and approach 41 °C away from the droplet. This is clearly in reasonable agreement with the experimentally measured values seen in figure 13.

6. Conclusions

We have investigated evolution of thin volatile droplets on a heated surface in a pure vapour environment both theoretically and experimentally. Our mathematical model accounts for the coupled effects of capillarity, thermocapillary stresses, evaporation,

heat conduction in the solid substrate, gravity, and disjoining pressure. A lubrication-type framework is employed to derive an evolution equation for the droplet thickness. The apparent contact line is defined as the transition region between the macroscopic droplet shape and the adsorbed film.

Numerical results for temperature profile under the droplet show a sharp temperature drop near the apparent contact line, suggesting that models based on the assumption of constant substrate temperature may not be appropriate for many practical situations. Our results also indicate that these models do not provide an accurate description of the role of thermocapillarity in droplet spreading.

Droplet dynamics depends on both heater power and wetting properties of the liquid. When a liquid is perfectly wetting under the isothermal conditions, nearly self-similar behaviour is seen when heater power is varied, but it breaks down when the effects of partial wetting are included. The latter result in different stages of evolution, with one of them corresponding to nearly constant wetted radius. Thus, we conclude that a situation very similar to classical contact line pinning can be encountered, as a result of the interplay between different components of disjoining pressure, even when the substrate is smooth and chemically homogeneous.

The experimental studies are conducted in a closed container filled with saturated vapour. Water droplets are deposited on a thin hydrophilic foil heater. The evolution of the droplet shape is observed with a CCD camera via the shadow method, while the temperature distribution below the droplet is measured simultaneously with a high resolution using thermochromic liquid crystals. Measurements of the apparent contact angle, diameter, height and volume of the droplet as well as the temperature distribution are obtained as the droplet evaporates.

The comparison between theory and experiment is very good, thus justifying the approach and opening up the possibility of using the model to understand a number of experimental results, including recent fascinating observations of interplay between evaporation and contact line instabilities (Poulard, Bénichou & Casabat 2003; Gotkis *et al*. 2006). Furthermore, the quantitative agreement between theory and experiment demonstrated in the present work allows one to use it for practical applications in heat transfer problems.

This work was supported by the Alexander von Humboldt Foundation and the NSF. The authors are grateful to Professor Ian Gladwell for valuable advice on numerical computations.

REFERENCES

Ajaev, V. S. 2005 Spreading of thin volatile liquid droplets on uniformly heated surfaces. *J. Fluid Mech.* **528**, 279–296.

Ajaev, V. S. & Homsy, G. M. 2001 Steady vapor bubbles in rectangular microchannels. *J. Colloid Interface Sci.* **240**, 259–271.

Anderson, D. M. & Davis, S. H. 1995 The spreading of volatile liquid droplets on heated surfaces. *Phys. Fluids* **7**, 248–265.

Bourgés-Monnier, C. & Shanahan, M. E. R. 1995 Influence of evaporation on contact angle. *Langmuir* **11**, 2820–2829.

Braun, R. J., Murray, B. T., Boettinger, W. J. & McFadden, G. B. 1995 Lubrication theory for reactive spreading of a thin drop. *Phys. Fluids* **7**, 1797–1810.

Brown, P. N., Byrne, G. D. & Hindmarsh, A. C. 1989 Vode: A variable coefficient ode solver. *SIAM J. Sci. Statist. Comput.* **10**, 1038–1051.

Burelbach, J. P., Bankoff, S. G. & Davis, S. H. 1988 Nonlinear stability of evaporating/condensing liquid films. *J. Fluid Mech.* **195**, 463–494.

Deegan, R. D., Bakajin, O., Dupont, T. F., Huber, G., Nagel, S. R. & Witten, T. A. 2000 Contact line deposits in an evaporating drop. *Phys. Rev.* E **62**, 756–765.

Derjaguin, B. V., Churaev, N. V. & Muller, V. M. 1987 *Surface Forces*. Plenum.

Freund, J. B. 2005 The atomistic detail of an evaporating meniscus. *Phys. Fluids* **17**, 022104.

de Gennes, P. G. 1985 Wetting: statics and dynamics. *Rev. Mod. Phys.* **57**, 827–863.

Gokhale, S. J., Plawsky, J. L. & Wayner, P. C. 2003 Experimental investigation of contact angle, curvature, and contact line motion in dropwise condensation and evaporation. *J. Colloid Interface Sci.* **259**, 354–366.

Gotkis, Y., Ivanov, I., Murisic, N. & Kondic, L. 2006 Dynamic structure formation at the fronts of volatile liquid drops. *Phys. Rev. Lett.* **93**, 186101.

Hocking, L. M. 1995 On contact angles in evaporating liquids. *Phys. Fluids* **7**, 2950–2955.

Höhmann, C. 2004 Temperaturmessverfahren zur räumlich hochauflösenden Untersuchung des Wärmetransports an einem verdampfenden Flüssigkeitsmeniskus. PhD thesis, Darmstadt University of Technology, Darmstadt.

Honig, C. D. F. & Ducker, W. A. 2007 No-slip hydrodynamic boundary condition for hydrophilic particles. *Phys. Rev. Lett.* **98**, 028305.

Hu, H. & Larson, R. G. 2005 Analysis of the microfluid flow in an evaporating sessile droplet. *Langmuir* **21**, 3963–3971.

Mollaret, R., Sefiane, K., Christy, J. R. E. & Veyret, D. 2004 Experimental and numerical investigation of the evaporation into air of a drop on a heated surface. *Trans. IChemE* A **82**, 471–480.

Moosman, S. & Homsy, G. M. 1980 Evaporating menisci of wetting fluids. *J. Colloid Interface Sci.* **73**, 212–223.

Potash, M. & Wayner, P. C. 1972 Evaporation from a two-dimensional extended meniscus. *Intl J. Heat Mass Transfer* **15**, 1851–1863.

Poulard, C., Bénichou, O. & Casabat, A. M. 2003 Freely receding evaporating droplets. *Langmuir* **19**, 8828–8834.

Rose, J. W. 2000 Accurate approximate equations for intensive sub-sonic evaporation. *Intl J. Heat Mass Transfer* **43**, 3869–3875.

Schrage, R. W. 1953 *A Theoretical Study of Interface Mass Transfer*. Columbia University Press.

Vinogradova, O. I. & Yakubov, G. E. 2003 Dynamic effects on force measurements. Part 2. Lubrication and the atomic force microscope. *Langmuir* **19**, 1227–1234.

Wong, H., Morris, S. & Radke, C. J. 1992 Three-dimensional menisci in polygonal capillaries. *J. Colloid Interface Sci.* **148**, 317–336.